PCCP

PAPER

View Article Online
View Journal | View Issue

Cite this: *Phys. Chem. Chem. Phys.*, 2024, **26**, 2218

Reactions of N_2O and CO on neutral $Rh_{10}O_n$ clusters: a density functional study†

Vikram Muman,[a] Alex Tennyson-Davies,[a] Oihan Allegret[ab] and Matthew A. Addicoat *[a]

Received 11th October 2023,
Accepted 9th December 2023

DOI: 10.1039/d3cp04929a

rsc.li/pccp

Density functional theory calculations were performed to identify product, reactant and intermediate dissociative/associative structures for the oxygen abstraction and addition reactions: $Rh_{10}O_n + CO \rightarrow Rh_{10}O_{n-1} + CO_2$, n = 1–5 and $Rh_{10}O_n + N_2O \rightarrow Rh_{10}O_{n+1} + N_2$, n = 0–4 reactions. In the case of the oxygen abstraction reactions, the energetics of the reaction path were very similar in energy regardless of the number of oxygen atoms on the $Rh_{10}O_n$ cluster, whereas for the addition of oxygen to the $Rh_{10}O_n$ cluster, the reaction was found to become significantly less exothermic with each successive addition of oxygen.

1 Introduction

Transition metal clusters have been of interest for several decades as both models of surfaces[1] and entities in their own right, where their remarkable size-[2] and structure-dependent[3–5] properties make them highly attractive as potential heterogeneous catalysts.[6–8] Late transition metal clusters, especially those of rhodium have maintained particular interest over that time with a multitude of studies employing a variety of spectroscopic and computational methods to probe their structure and behaviour.

Many of these studies have been motivated by the use of rhodium in automotive three-way catalytic converters[9] and the reactions of N_2O,[10–12] NO,[13–22] CO[23,24] and CO_2[25] have been extensively investigated on both pure and doped[26–28] rhodium clusters. Given that spectroscopic methods such as infrared multiple photon dissociation spectroscopy (IRMPD)[29] use mass spectroscopy to identify the species of interest, they generally provide information only about the products of reactions and reactivity studies therefore often include computational investigation,[30,31] typically using density functional theory (DFT), but sometimes including higher level methods such as CCSD(T).[32]

Two particular reactions that are of interest for automotive catalytic converters are the reduction of NO_x to N_2 and the oxidation of CO to CO_2. Both of these reactions have specifically been investigated on rhodium[11,26] and platinum[33,34] clusters. Aviles *et al.* undertook calculations to elucidate the N_2O reduction mechanism on small Rh_n clusters (n = 2–4), and determined that the N_2–O bond was readily broken by the Rh_n cluster, but the N_2 bond was not.[12] Yamamoto *et al.* used both IRMPD and DFT methods to determine reaction paths for the reduction of N_2O by Pt_6 and Pt_7 clusters.,[35] while Hernández and coworkers used DFT to elucidate the reaction of N_2O on Pt_8.[36]

Yet despite these successes, computational investigation remains challenging, especially on large and/or late transition metal clusters: Even employing frozen core/effective core potential approaches, clusters still possess a large number of electrons. A wide range of spin multiplicities need to be considered. And many clusters have multiple, very different geometries that all occur within a small energetic range,[5,37,38] that is thermally accessible and/or within the error of computational methods. For some clusters, the manifold of low-energy geometries may be so dense and the ease of interconversion so facile, that the clear identification of a ground state is challenging. Rh_{10} has been identified as one such fluxional molecule.[39] Such a dense manifold of structures, energies and spin multiplicities is additionally challenging when employing reaction path following methods such as Quasi-Synchronous transit and intrinsic reaction coordinate methods, as reaction paths may follow a comparatively broad path, where spin and cluster geometry may differ throughout a reaction.

In 2012, Yamada *et al.* undertook a mass-spectroscopic study on neutral rhodium clusters, Rh_n (n = 10–28).[40] By injecting both N_2O and CO into their cluster source, they were able to demonstrate a full catalytic cycle and observed that the distribution of oxide products Rh_nO_m was determined by an equilibrium between the oxygen being transferred to the Rh_nO_m

[a] *School of Science and Technology, Nottingham Trent University, Clifton Lane, Nottingham, NG11 8NS, UK. E-mail: matthew.addicoat@ntu.ac.uk*
[b] *Univ Limoges, IRCER, UMR CNRS 7315, F-87068 Limoges, France*

† Electronic supplementary information (ESI) available: Spreadsheet of reaction path energies, zipfile of reaction path structures. Structures are additionally available at https://zenodo.org/record/8428605. See DOI: https://doi.org/10.1039/d3cp04929a

m = 0–4 cluster from N_2O and oxygen being abstracted from the Rh_nO_m m = 1–5, and that the rate constants for the oxygen abstraction reaction were 2–3 orders of magnitude higher on clusters where $m \geq 4$ than those clusters with three or less oxygen atoms. They concluded that oxidized rhodium clusters were more effective as catalysts compared to bare clusters. Yamada's study used experimentally derived rate constants and did not include any calculated structures or reaction paths. Indeed the size of the rhodium clusters employed by Yamada *et al.*, Rh_n (n = 10–28) makes DFT challenging.

In this work, we revisit the catalytic cycle presented by Yamada *et al.* for the smallest rhodium cluster size, Rh_{10}. As reaction path following on such flat potential energy surfaces (PES) is difficult, we employ a fully stochastic search procedure followed by DFT calculations to identify the reactants, products and the bond forming/breaking intermediate for both the oxygen transfer and oxygen abstraction reactions on the Rh_{10} cluster.

2 Computational method

The geometry of Rh_{10} was determined using the Kick[3] stochastic structure generator supplied with 10 Rh atoms.[41,42] Following optimization, the lowest energy Rh_{10} geometry was then employed as a fragment in further Kick[3] runs with n oxygen atoms in order to determine the lowest energy $Rh_{10}O_n$ structures, for n = 1–5. A key point on each $Rh_{10}O_n \rightarrow Rh_{10}O_{n\pm1}$ reaction path, is the species where the $N_2\cdots O$ bond is being broken, or where the $O\cdots CO$ bond is being formed. To identify these intermediate species directly, N_2O and OCO fragments with elongated NO and CO bonds respectively, were used as input to Kick[3] to identify the $Rh_{10}O_n$ CO and $Rh_{10}O_n$ N_2 intermediate species. 1000 stochastic geometries were generated for each stoichiometry.

The stochastically generated structures were optimized in a two-stage procedure: Firstly using the semi-empirical GFN1-xTB method,[43] maintaining the geometry of all fragments employed in the stochastic structure generation, before a full optimization using BP86/DZP and then re-optimization using the TZ2P basis set. Up to the 4p electrons of rhodium were treated using a frozen core. Structures were initially optimized in the octet multiplicity before re-optimization with each multiplicity from doublet to 20-tet. 18- and 20-tet structures were found to lie very high in energy and were consequently not considered in analysis. All calculations were undertaken using AMS2022.1 using scalar relativivity and applying an electronic temperature of 373.15 K.[44]

To confirm that the BP86[45,46] functional is sufficient, we also tested the TPSS[47] functional with the D3(BJ)[48,49] dispersion correction. The choice of functional made no significant difference to the relative ordering of different multiplicity $Rh_{10}O_n$ structures, as shown by difference-of-difference values in the ESI.† GGA functionals are expected to only give qualitative information about barrier heights, due to their self-interaction error[50] and this is evident, with BP86 intermediate relative energies for oxygen abstraction reactions being consistently $\approx$0.4 eV higher in energy than the TPSS-calculated values and BP86 product energies being consistently $\approx$0.5 eV lower than the TPSS-calculated values. For the oxygen addition reaction paths, the TPSS relative energies for intermediate and product species are lowered w.r.t. the BP86 paths by $\approx$0.6 and 0.3 eV respectively.

After optimization of $Rh_{10}O_n$, $Rh_{10}O_n$ CO and $Rh_{10}O_n$ N_2 structures, $Rh_{10}O_n \rightarrow Rh_{10}O_{n\pm1}$ reaction paths were determined by geometric RMSD. For each reaction, the lowest energy $Rh_{10}O_n$ reactant was chosen, and the nearest $Rh_{10}O_{\pm1}$ geometric match was determined ($Rh_{10}O_{n+1}$ for $Rh_{10}O_n + N_2O \rightarrow Rh_{10}O_{n+1} + N_2$ and $Rh_{10}O_{n-1}$ for $Rh_{10}O_n + CO \rightarrow Rh_{10}O_{n-1} + CO_2$). The intermediate species was determined in the same manner, by determining the RMSD with the reactant and then confirming RMSD with the product. After the addition of the first two oxygen atoms to Rh_{10}, multiple oxygen abstraction reaction paths are possible, corresponding to abstraction of different oxygen atoms, the path presented in this work is the one containing the most favourable (lowest energy) intermediate geometry.

It is not necessarily the case that the lowest energy $Rh_{10}O_n$ will lead to the lowest energy $Rh_{10}O_{n\pm1}$ species, and because of the circular nature of the catalytic reaction, each $Rh_{10}O_n$ species appears as both a product and a reactant. Therefore, a second reaction path, beginning with the lowest energy reactant was also determined following the same geometric RMSD procedure. We denote the two reaction paths as lowest energy reactant (LER) and lowest energy product (LEP).

3 Results and discussion

Rh_{10}

Several computational[38,51] and experimental studies have investigated the structure of the Rh_{10} cluster in neutral, cationic and anionic charge states, identifying a dense manifold of low-energy structures. Knickelbein *et al.* measured the static electric dipole polarizabilities of Rh_n n = 5–28 clusters and suggested that Rh_{10} is a fluxional molecule.[39] The lowest energy Rh_{10} octet species identified in this work is a structure with C_{2v} symmetry and a binding energy of −1.7686006 a.u. and is shown in Fig. 1. Re-optimization of each identified Rh_{10} isomer at other multiplicities (doublet to 20-tet) revealed the lowest energy isomer overall, is the same structure, but with 16-tet

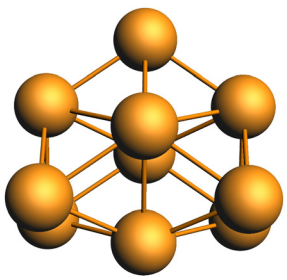

Fig. 1 Lowest energy geometry of Rh_{10}.

multiplicity and a binding energy of −1.7909319 a.u. This structure corresponds to the sc3 structure identified for Rh_{10}^+ by Harding *et al.*[51]

$Rh_{10}O_n + CO \rightarrow Rh_{10}O_{n-1} + CO_2$ reactions

$Rh_{10}O + CO \rightarrow Rh_{10} + CO_2$. Only the predetermined minimum Rh_{10} structure is considered in this work, therefore there is only one $Rh_{10}O + CO \rightarrow Rh_{10} + CO_2$ reaction path, defined by the lowest energy $Rh_{10}O$ species, which has a μ^2-bound oxygen. The reaction path from this species is shown in Fig. 2. The $Rh_{10}O\cdots C$ distance in the intermediate state is 2.72 Å. Overall, the reaction path is very flat with the separated products ($Rh_{10} + CO_2$) lying only 0.15 eV above the reactants and the intermediate $Rh_{10}O\cdots CO$ structure being effectively isoenergetic with the $Rh_{10}O$ + CO reactants. For the reactant and intermediate structures, all multiplicities (doublet to 16-tet) were found within a range of 0.35 eV. Different multiplicities of the Rh_{10} product span an energetic range of 0.71 eV.

$Rh_{10}O_2 + CO \rightarrow Rh_{10}O + CO_2$. Both the LER (Fig. 3) and LEP (Fig. 4) reaction paths arrive at the same μ^2 $Rh_{10}O$ product – *i.e.* the lowest energy $Rh_{10}O_2$ can follow a reaction path that results in the lowest energy $Rh_{10}O$. The lowest energy $Rh_{10}O_2$ structure has two μ^2-bound oxygen atoms in symmetry-equivalent positions. The intermediate CO-bound species, removing either of these oxygen atoms is −1.93 eV lower in energy than the separated reactants and has a $Rh_{10}O\cdots C$ distance of 3.19 Å.

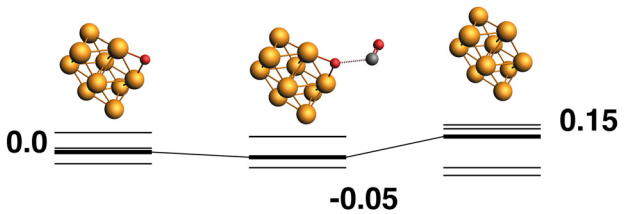

Fig. 2 $Rh_{10}O + CO \rightarrow Rh_{10} + CO_2$ reaction path for the lowest energy $Rh_{10}O$ species. Relative energies are shown for the octet surface in eV. The octet surface is bolded, all other multiplicities are shown with thin lines.

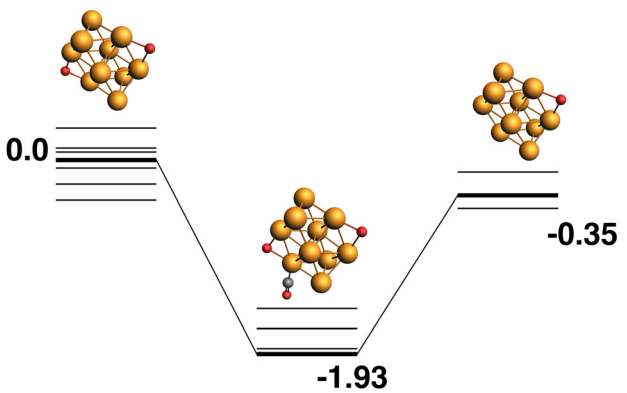

Fig. 3 $Rh_{10}O_2 + CO \rightarrow Rh_{10}O + CO_2$ reaction path for the lowest energy $Rh_{10}O_2$ species. Relative energies are shown for the octet surface in eV. The octet surface is bolded, all other multiplicities are shown with thin lines.

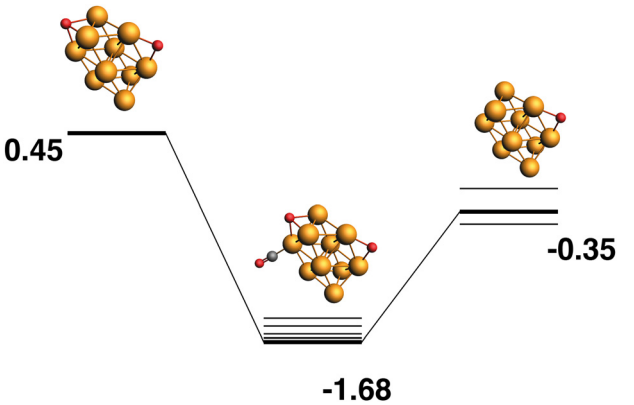

Fig. 4 $Rh_{10}O_2 + CO \rightarrow Rh_{10}O + CO_2$ reaction path for the lowest energy product ($Rh_{10}O$) species. Relative energies are shown for the octet surface in eV. Zero energy is the lowest energy $Rh_{10}O_2$ reactant, as shown in Fig. 3. The octet surface is bolded, all other multiplicities are shown with thin lines.

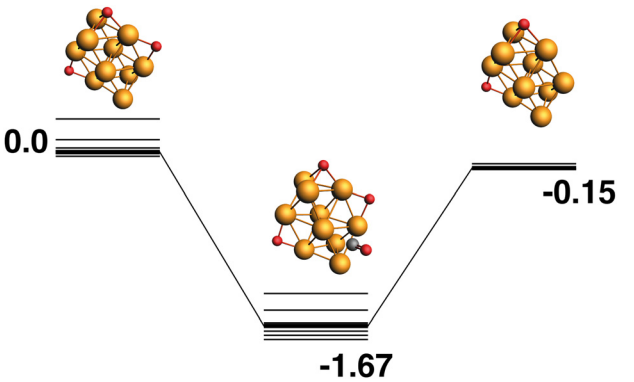

Fig. 5 $Rh_{10}O_3 + CO \rightarrow Rh_{10}O_2 + CO_2$ reaction path for the lowest energy $Rh_{10}O_3$ species. Relative energies are shown for the octet surface in eV. The octet surface is bolded, all other multiplicities are shown with thin lines.

Beginning with the lowest energy μ^2 $Rh_{10}O$ product and searching for a reaction path towards any $Rh_{10}O_2$ reactant, yields a $\mu^3\mu^2$ reactant 0.45 eV higher in energy than the lowest energy $Rh_{10}O_2$ and a corresponding $Rh_{10}OO{\cdot}CO$ intermediate. The intermediate structure removes the μ^3-bound oxygen atom and is at −1.68 eV, 0.25 eV higher in energy than the intermediate in the LER pathway.

$Rh_{10}O_3 + CO \rightarrow Rh_{10}O_2 + CO_2$. The reaction path from the lowest energy $Rh_{10}O_3$ structure is shown in Fig. 5. The lowest energy $Rh_{10}O_3$ structure has the same two μ^2-bound oxygen atoms as in $Rh_{10}O_2$ plus a μ^3-bound oxygen atom that shares a Rh atom with one of the μ^2-bound oxygen atoms. In the $Rh_{10}O_2O{\cdot}CO$ intermediate structure, the incoming CO approaches the side of the cluster with both the μ^3 and μ^2 oxygen atoms, but abstracts the μ^2-bound oxygen. The intermediate is at −1.67 eV and the $Rh_{10}O\cdots C$ distance is 3.39 Å. The $Rh_{10}O_2$ product is at −0.15 eV. Removal of the μ^3-bound oxygen instead of the μ^2-bound oxygen yields the lowest energy $Rh_{10}O_2$ structure at −0.59 eV, and this pathway is shown in Fig. 6. The intermediate in

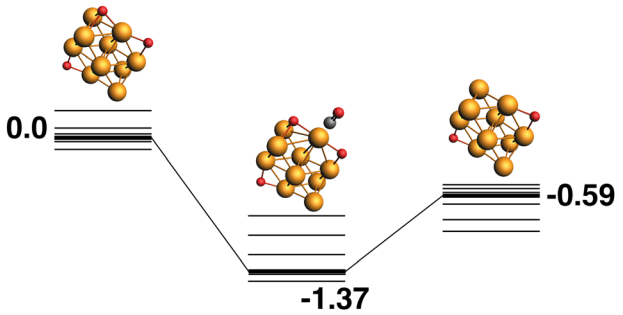

Fig. 6 $Rh_{10}O_3$ + CO → $Rh_{10}O_2$ + CO_2 reaction path for the lowest energy product ($Rh_{10}O_2$) species. Relative energies are shown for the octet surface in eV. Zero energy is the lowest energy $Rh_{10}O_3$ reactant, as shown in Fig. 5. The octet surface is bolded, all other multiplicities are shown with thin lines.

this pathway is at −1.37 eV, 0.30 eV higher in energy than the LER path intermediate and the $Rh_{10}O\cdots C$ distance is 2.91 Å.

$Rh_{10}O_4$ + CO → $Rh_{10}O_3$ + CO_2. The lowest energy $Rh_{10}O_4$ structure has three μ^3 -bound oxygen atoms and a μ^2-bound oxygen. The reaction path from this species is shown in Fig. 7 and removes one of the μ^3 oxygen atoms. The products ($Rh_{10}O_3$ + CO_2) are nearly isoenergetic with the reactants. As the oxygen atoms in the $Rh_{10}O_4$ cluster are all bound (in part) to the same four Rh atoms, the approaching CO is likely to interact with more than one oxygen atom. In the lowest energy intermediate structure identified, the CO could possibly abstract one of two a μ^3-bound oxygen atoms, with $Rh_{10}O\cdots C$ distances of 3.08 and 3.22 Å respectively.

The lowest energy $Rh_{10}O_3$, as above, possesses two μ^2-bound oxygen atoms and one μ^3-bound oxygen, so it is not a possible product (without rearrangement) from the lowest energy $Rh_{10}O_4$ structure. The path ending with the lowest energy $Rh_{10}O_3$ structure beings with a high energy $Rh_{10}O_4$ structure (+1.25 eV), which has two μ^3-bound oxygen atoms and two μ^2-bound oxygen atoms (Fig. 8). The close $Rh_{10}O\cdots C$ distances in the intermediate structure, are 3.16 Å for the μ^3-bound oxygen that is abstracted by the CO and 3.39 Å for the μ^2-bound oxygen that remains.

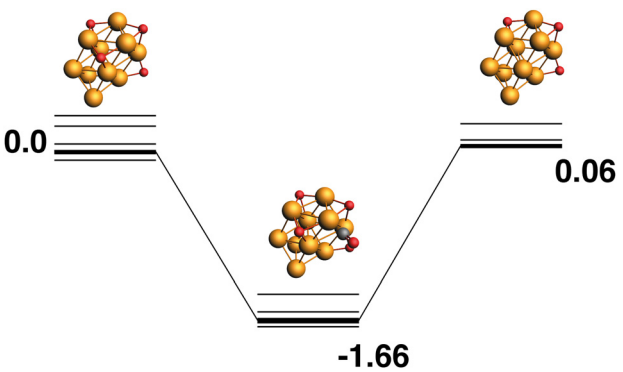

Fig. 7 $Rh_{10}O_4$ + CO → $Rh_{10}O_3$ + CO_2 reaction path for the lowest energy $Rh_{10}O_4$ species. Relative energies are shown for the octet surface in eV. The octet surface is bolded, all other multiplicities are shown with thin lines.

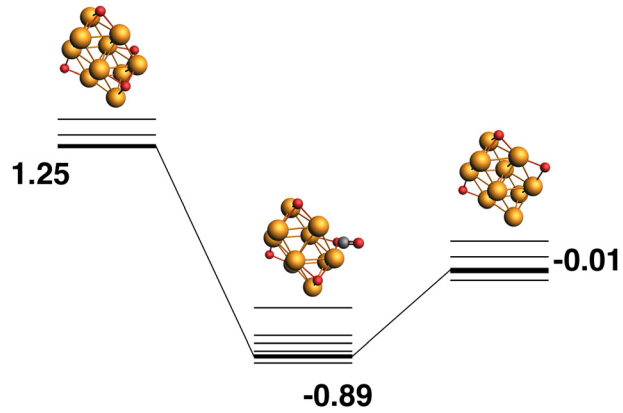

Fig. 8 $Rh_{10}O_4$ + CO → $Rh_{10}O_3$ + CO_2 reaction path for the lowest energy product ($Rh_{10}O_3$) species. Relative energies are shown for the octet surface in eV. Zero energy is the lowest energy $Rh_{10}O_4$ reactant, as shown in Fig. 7. The octet surface is bolded, all other multiplicities are shown with thin lines.

$Rh_{10}O_5$ + CO → $Rh_{10}O_4$ + CO_2. The lowest energy $Rh_{10}O_5$ structure has four μ^3-bound oxygen atoms and a μ^2-bound oxygen. The reaction path from this species is shown in Fig. 9 and removes one of the μ^3 oxygen atoms. Similarly to the $Rh_{10}O_4$ to $Rh_{10}O_3$ LER reaction path, the products ($Rh_{10}O_4$ + CO_2) are nearly isoenergetic with the reactants, the relative energy of the $Rh_{10}O_5$·CO intermediate species is also similar to that of the $Rh_{10}O_4$·CO intermediate (Fig. 7), at −1.61 eV. The approaching CO abstracts a μ^3 -bound oxygen atom from 3.04 Å.

The LEP reaction path is shown in Fig. 10. The $Rh_{10}O_4$ product has a relative energy of −0.96 eV and the lowest energy reaction path removes a μ^1-bound oxygen atom that is bound to a previously bare Rh atom.

$Rh_{10}O_n$ + N_2O → $Rh_{10}O_{n+1}$ + N_2 reactions

Rh_{10} + N_2O → $Rh_{10}O$ + N_2. Only the predetermined minimum Rh_{10} structure is considered in this work, therefore there is only one Rh_{10} + N_2 → $Rh_{10}O$ + N_2 reaction path, defined by

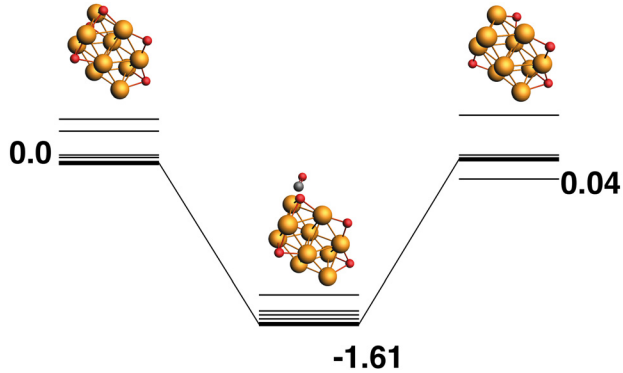

Fig. 9 $Rh_{10}O_5$ + CO → $Rh_{10}O_4$ + CO_2 reaction path for the lowest energy $Rh_{10}O_5$ species. Relative energies are shown for the octet surface in eV. The octet surface is bolded, all other multiplicities are shown with thin lines.

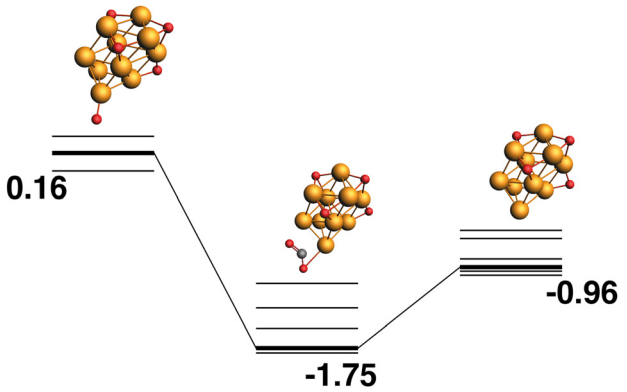

Fig. 10 $Rh_{10}O_5$ + CO → $Rh_{10}O_4$ + CO_2 reaction path for the lowest energy product ($Rh_{10}O_4$) species. Relative energies are shown for the octet surface in eV. Zero energy is the lowest energy $Rh_{10}O_5$ reactant, as shown in Fig. 9. The octet surface is bolded, all other multiplicities are shown with thin lines.

the lowest energy $Rh_{10}O$ species, which has a μ^2-bound oxygen. The reaction path from this species is shown in Fig. 11. The energetic profile of the reaction path is quite different from the reduction reactions, with the $Rh_{10}O.N_2$ intermediate structure being −4.54 eV below zero energy and the $Rh_{10}O$ + N_2 products being found at −3.57 eV. The $Rh_{10}O{\cdot}N_2$ separation is 3.07 Å.

$Rh_{10}O$ + N_2O → $Rh_{10}O_2$ + N_2. The lowest energy $Rh_{10}O$ structure, as previously seen, has a μ^2-bound oxygen. The reaction path from this species is shown in Fig. 12 and deposits a μ^3 oxygen atom such that no Rh atoms bind both oxygen atoms. The intermediate structure has a relative energy of

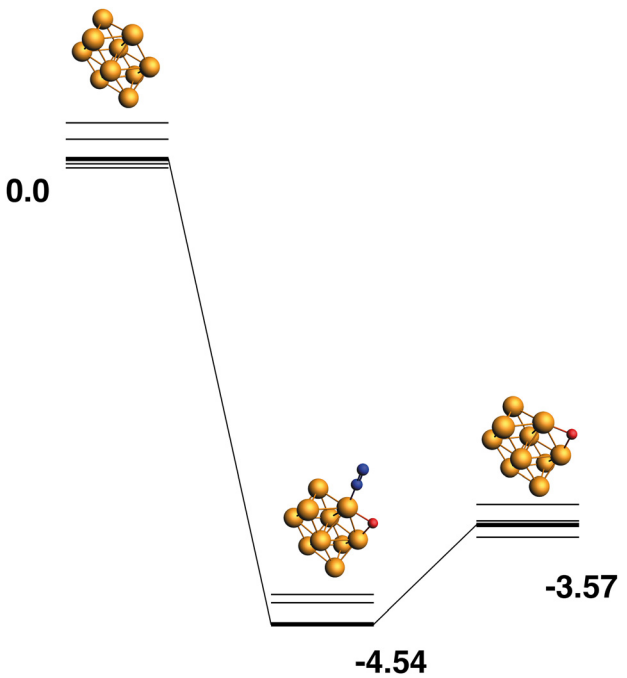

Fig. 11 Rh_{10} + N_2O → $Rh_{10}O$ + N_2 reaction path for the lowest energy product ($Rh_{10}O$) species. Relative energies are shown for the octet surface in eV. Zero energy is the defined Rh_{10} reactant, as shown in Fig. 1. The octet surface is bolded, all other multiplicities are shown with thin lines.

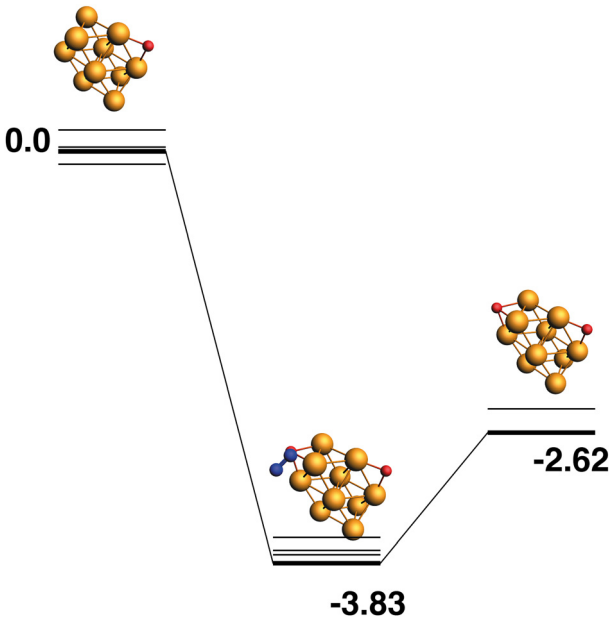

Fig. 12 $Rh_{10}O$ + N_2O → $Rh_{10}O_2$ + N_2 reaction path for the lowest energy $Rh_{10}O$ species. Relative energies are shown for the octet surface in eV. The octet surface is bolded, all other multiplicities are shown with thin lines.

−3.83 eV and the $Rh_{10}O{\cdot}N_2$ distance is 3.96 Å. The products are found at −2.62 eV.

The LEP reaction path is shown in Fig. 13. The $Rh_{10}O_2$ product has a relative energy of −3.07 eV and deposits the second of the two symmetry-equivalent μ^2-bound oxygen atoms.

$Rh_{10}O_2$ + N_2O → $Rh_{10}O_3$ + N_2. Both the LER (14) and LEP (15) reaction paths form the lowest energy $Rh_{10}O_3$ product, which has two μ^2 and one μ^3-bound oxygen atom. This product ($Rh_{10}O_2$ + N_2) has an energy of −2.83 eV relative to the lowest energy $Rh_{10}O_2$ + N_2O. The intermediate structure connecting

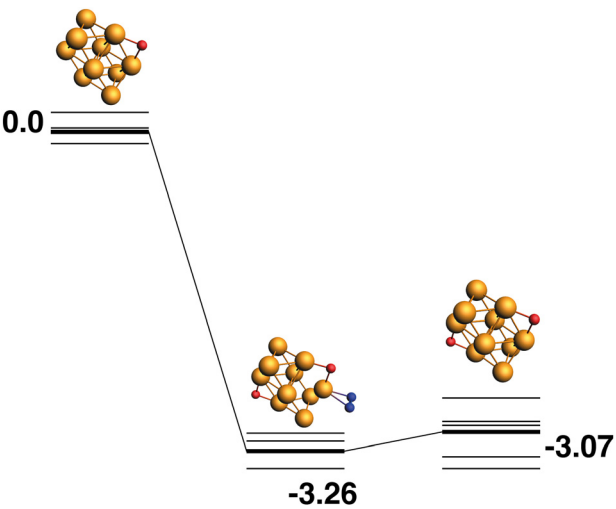

Fig. 13 $Rh_{10}O$ + N_2O → $Rh_{10}O_2$ + N_2 reaction path for the lowest energy product ($Rh_{10}O_2$) species. Relative energies are shown for the octet surface in eV. Zero energy is the lowest energy $Rh_{10}O$ reactant, as shown in Fig. 12. The octet surface is bolded, all other multiplicities are shown with thin lines.

these two lowest energy $Rh_{10}O_2$ and $Rh_{10}O_3$ structures, must therefore deposit the μ^3 -bound oxygen atom. This intermediate is found at −3.83 eV and the $Rh_{10}O{\cdot}N_2$ distance is 3.96 Å. If instead, of depositing the μ^3 -bound oxygen atom, the intermediate is chosen to deposit one of the two μ^2-oxygen atoms, the reaction path in Fig. 15 is observed. The $Rh_{10}O_2$ reactant and $Rh_{10}O_3{\cdot}N_2$ intermediate structures are found at +0.44 and −3.83 eV respectively - *i.e.* the intermediate structure is 0.3 eV higher in energy than the LER intermediate and has a $Rh_{10}O{\cdot}N_2$ distance of 2.99 Å.

$Rh_{10}O_3 + N_2O \rightarrow Rh_{10}O_4 + N_2$. The LER reaction path for the $Rh_{10}O_3 + N_2O \rightarrow Rh_{10}O_4 + N_2$ reaction is shown in Fig. 16. The $Rh_{10}O_4$ product at −2.16 eV has two μ^2 and two μ^3-bound oxygen atoms and the corresponding intermediate structure at −3.23 eV has a $Rh_{10}O{\cdot}N_2$ distance of 3.20 Å, depositing the second μ^3 oxygen atom. The path leading to the lowest energy $Rh_{10}O_4$ product is shown in Fig. 17. The $Rh_{10}O_4$ product has three μ^3 and one μ^2-bound oxygen atom, and the lowest energy intermediate structure deposits the third μ^3-bound oxygen atom. The geometrically matching $Rh_{10}O_3$ reactant with two μ^3 and one μ^2-bound oxygen, is very close in energy to the lowest energy $Rh_{10}O_3$ structure (two × μ^3 and 1 × μ^2), with a relative energy of only 0.07 eV. The $Rh_{10}O{\cdot}N_2$ distance in the intermediate structure is 3.56 Å.

$Rh_{10}O_4 + N_2O \rightarrow Rh_{10}O_5 + N_2$. The reaction path from the lowest energy $Rh_{10}O_4$ structure is shown in Fig. 18. The $Rh_{10}O_5$ product lies at −2.41 eV has two μ^2 and three μ^3-bound oxygen atoms and the corresponding intermediate structure, depositing the second μ^2 oxygen atom, lies very close in energy at −2.48 eV and has a $Rh_{10}O{\cdot}N_2$ distance of 3.38 Å. The lowest energy $Rh_{10}O_5$ structure has one μ^2 and four μ^3-bound oxygen atoms and the path leading to this product is shown in Fig. 19. The lowest energy matching intermediate structure at −3.75 eV corresponds to depositing the fourth μ^3-bound oxygen atom, but the corresponding $Rh_{10}O_4$ reactant is high in energy, at +1.00 eV. The $Rh_{10}O{\cdot}N_2$ distance in the intermediate structure is 3.94 Å.

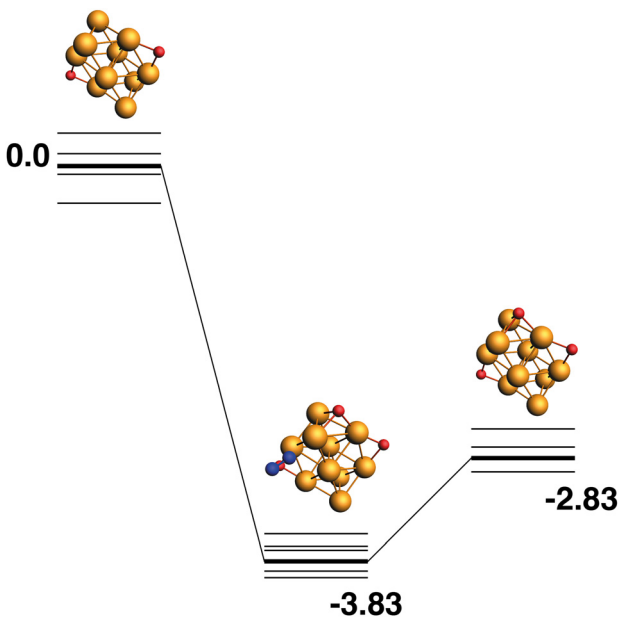

Fig. 14 $Rh_{10}O_2 + N_2O \rightarrow Rh_{10}O_3 + N_2$ reaction path for the lowest energy $Rh_{10}O_2$ species. Relative energies are shown for the octet surface in eV. The octet surface is bolded, all other multiplicities are shown with thin lines.

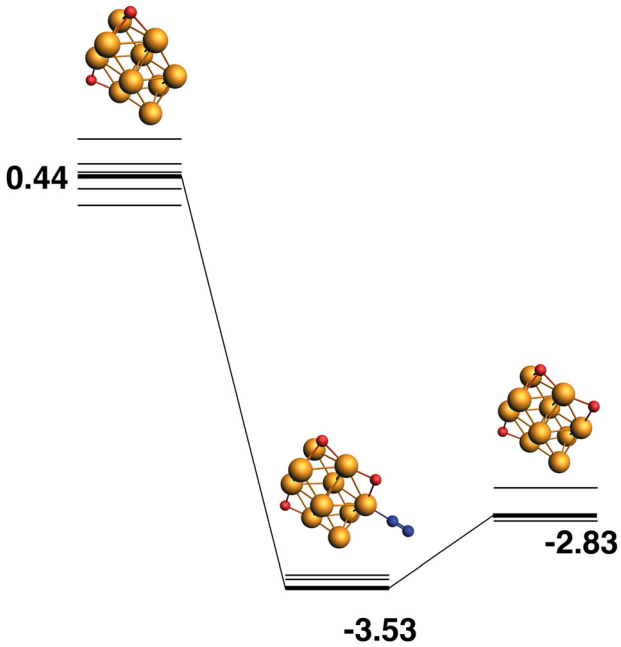

Fig. 15 $Rh_{10}O_2 + N_2O \rightarrow Rh_{10}O_3 + N_2$ reaction path for the lowest energy product ($Rh_{10}O_3$) species. Relative energies are shown for the octet surface in eV. Zero energy is the lowest energy $Rh_{10}O_2$ reactant, as shown in Fig. 14. The octet surface is bolded, all other multiplicities are shown with thin lines.

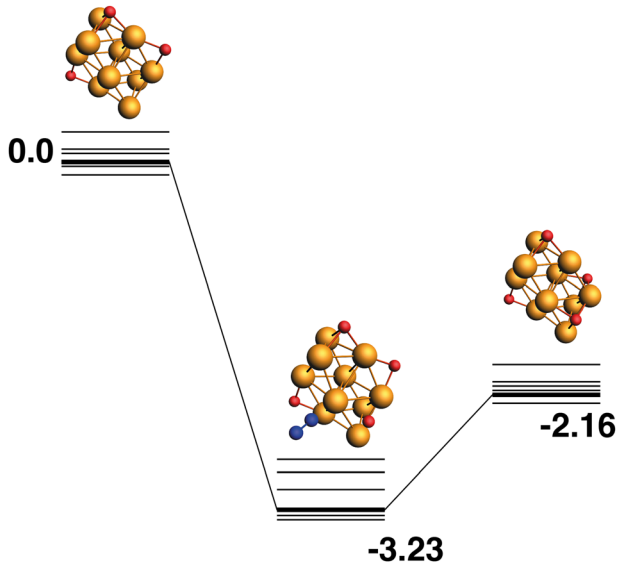

Fig. 16 $Rh_{10}O_3 + N_2O \rightarrow Rh_{10}O_4 + N_2$ reaction path for the lowest energy $Rh_{10}O_3$ species. Relative energies are shown for the octet surface in eV. The octet surface is bolded, all other multiplicities are shown with thin lines.

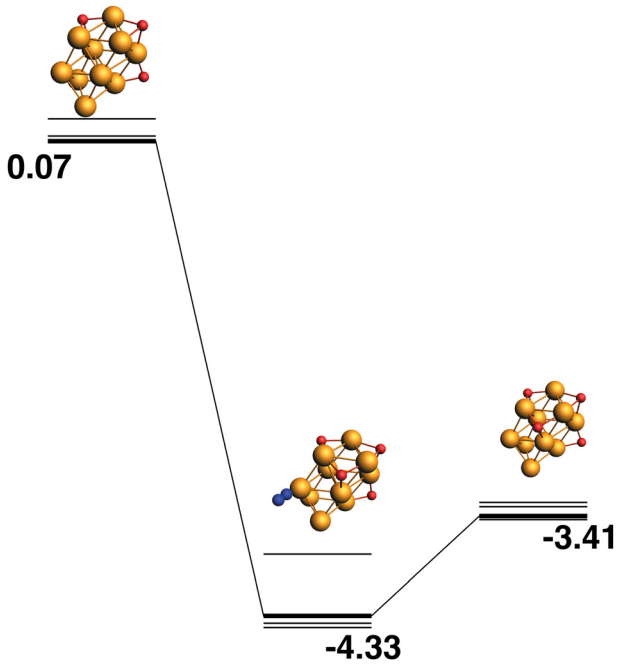

Fig. 17 $Rh_{10}O_3 + N_2O \rightarrow Rh_{10}O_4 + N_2$ reaction path for the lowest energy product ($Rh_{10}O_4$) species. Relative energies are shown for the octet surface in eV. Zero energy is the lowest energy $Rh_{10}O_3$ reactant, as shown in Fig. 16. The octet surface is bolded, all other multiplicities are shown with thin lines.

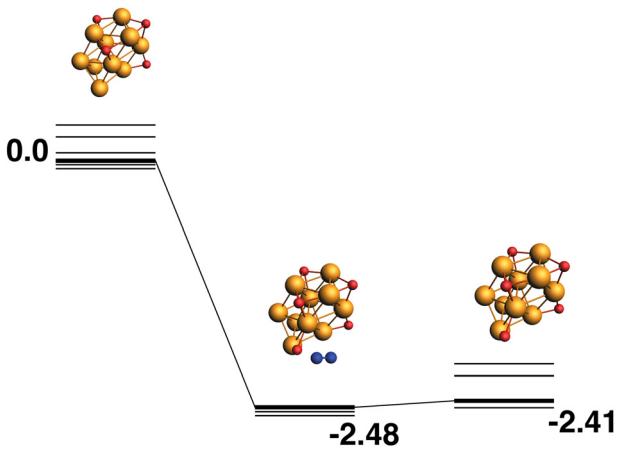

Fig. 18 $Rh_{10}O_4 + N_2O \rightarrow Rh_{10}O_5 + N_2$ reaction path for the lowest energy $Rh_{10}O_4$ species. Relative energies are shown for the octet surface in eV. The octet surface is bolded, all other multiplicities are shown with thin lines.

Comparison of the $Rh_{10}O_n + CO \rightarrow Rh_{10}O_{n-1} + CO_2$ reaction paths for n = 1–5 reveals a largely similar energetic landscape regardless of n, as shown in Fig. 20 and 21 for the LER and LEP reaction paths respectively. For the pathways beginning with the lowest energy reactant, with the exception of the last abstraction of oxygen, resulting in a bare rhodium cluster (*i.e.* $Rh_{10}O + CO \rightarrow Rh_{10}O + CO_2$, Fig. 2), where the intermediate structure lies very close to the energy of both the products and

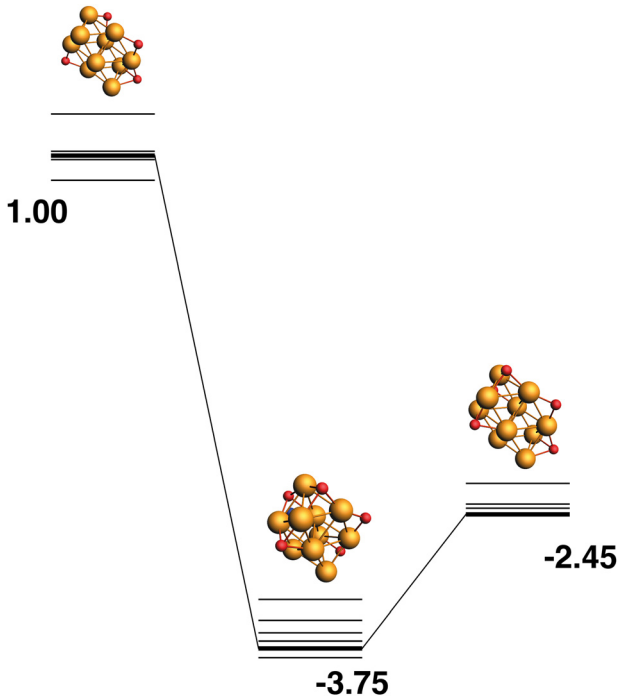

Fig. 19 $Rh_{10}O_4 + N_2O \rightarrow Rh_{10}O_5 + N_2$ reaction path for the lowest energy product ($Rh_{10}O_5$) species. Relative energies are shown for the octet surface in eV. Zero energy is the lowest energy $Rh_{10}O_4$ reactant, as shown in Fig. 18. The octet surface is bolded, all other multiplicities are shown with thin lines.

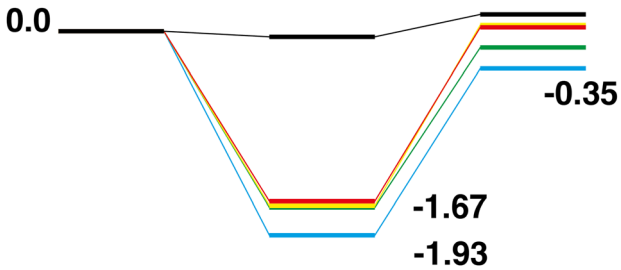

Fig. 20 $Rh_{10}O_n + CO \rightarrow Rh_{10}O_{n-1} + CO_2$, n = 1–5 LER reaction paths overlaid. The $Rh_{10}O + CO_2$ path is black, the $Rh_{10}O_n$ paths are coloured blue, green, yellow and red, for n = 2–5 respectively.

reactants, the four reaction paths have almost the same energetics, with the $Rh_{10}O_n{\cdot}CO$ intermediate structure being found in a narrow range between −1.67 and −1.93 eV relative to the reactants. The $Rh_{10}O_{n-1}$ products are found in a similarly narrow energy range, from −0.35 eV for the $Rh_{10}O_2$ reaction to +0.06 eV for the $Rh_{10}O_4$ reaction. Considering the reaction paths arriving at the lowest energy products, shows similar behaviour, with intermediate structures consistently 2 eV lower in energy than the corresponding reactants. The ΔE (products-reactants) shows some deviation with values of 0.80, 0.59, 1.26 and 1.17 eV for n = 2–5 respectively, indicating that the $Rh_{10}O_{n-1}$ products are more stable for the $Rh_{10}O_4$ and $Rh_{10}O_5$ reactants. This is consistent with the higher rates observed for the $Rh_mO_n + CO \rightarrow Rh_mO_{n-1} + CO_2$ reactions for n = 4,5 by Yamada *et al.*[40]

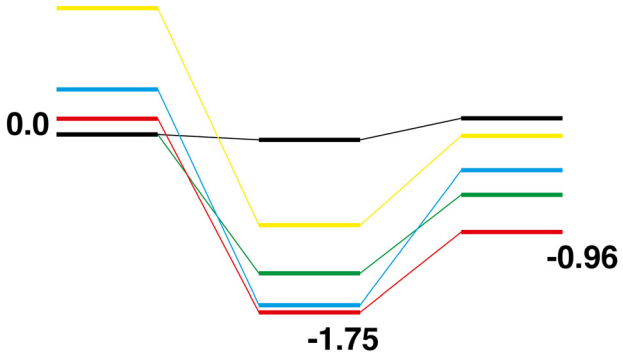

Fig. 21 $Rh_{10}O_n$ + CO → $Rh_{10}O_{n-1}$ + CO_2, n = 1–5 LEP reaction paths overlaid. Zero energy is the lowest energy $Rh_{10}O$ reactant, as shown in Fig. 2. The $Rh_{10}O$ + CO_2 path is black, the $Rh_{10}O_n$ paths are coloured blue, green, yellow and red, for n = 2–5 respectively.

Comparison of the $Rh_{10}O_n$ + N_2O → $Rh_{10}O_{n+1}$ + N_2 reaction paths for n = 0–4, shows a very different pattern to the abstraction of oxygen reactions. Considering first the LER paths, shown overlaid in Fig. 22. As the $Rh_{10}O_n$ reactant is increasingly oxidized (*i.e.* as n increases), the relative energy of both the intermediate and product increases. With increasing oxygen content, the energy of the intermediate species rises by approximately 0.7 eV. The relative energy of the $Rh_{10}O_{n+1}$ product also rises, but less linearly, with the $Rh_{10}O_4$ and $Rh_{10}O_5$ products switching order. A change in behaviour is clearly seen for the $Rh_{10}O_4$ + N_2O → $Rh_{10}O_5$ + N_2 reaction, where the intermediate and product species are almost isoenergetic, compared to the n = 0–3 reactions, where the products are less stable than the intermediate by approximately 1 eV. The LEP reaction paths, shown overlaid in Fig. 23 show broadly similar energy profiles. The most notable feature is the difference in the relative energies of the intermediate and product species, which

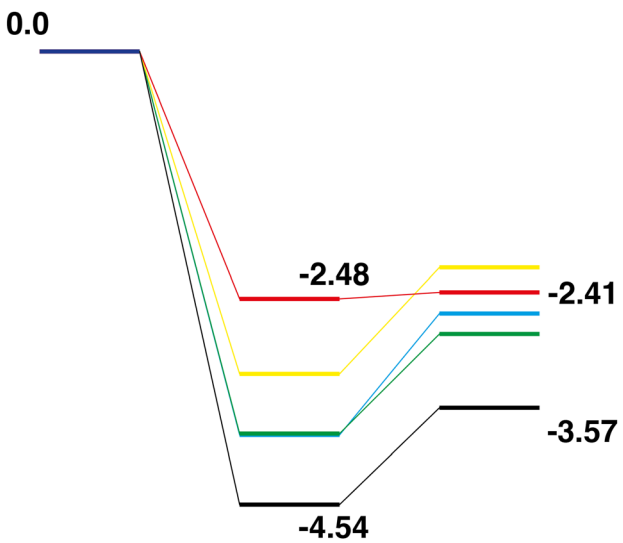

Fig. 22 $Rh_{10}O_n$ + N_2O → $Rh_{10}O_{n+1}$ + N_2, n = 0–4 LER reaction paths overlaid. The Rh_{10} + N_2O path is black, the $Rh_{10}O_n$ paths are coloured blue, green, yellow and red, for n = 1–4 respectively.

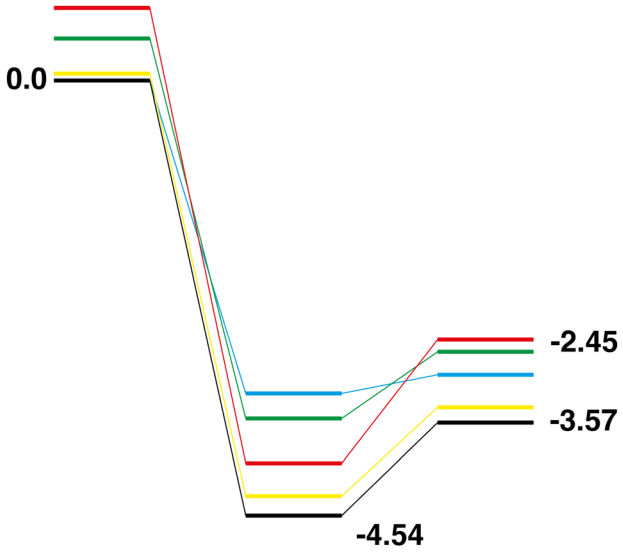

Fig. 23 $Rh_{10}O_n$ + N_2O → $Rh_{10}O_{n+1}$ + N_2, n = 0–4 LEP reaction paths overlaid. Zero energy is the lowest energy Rh_{10} reactant, as shown in Fig. 11. The Rh_{10} + N_2O path is black, the $Rh_{10}O_n$ paths are coloured blue, green, yellow and red, for n = 1–4 respectively.

increases from 0.195 eV for the $Rh_{10}O$ + N_2 reaction, to 0.71, 0.93 and 1.29 eV for the n = 2–4 paths respectively.

4 Conclusion

We have determined the key points on the reaction paths of $Rh_{10}O_n$ + CO → $Rh_{10}O_{n-1}$ + CO_2 and $Rh_{10}O_n$ + N_2O → $Rh_{10}O_{n+1}$ + N_2 reactions at multiplicities ranging from doublet up to 16-tet. The vast majority of structures were found to lie within a relatively small energetic range, indicating that most multiplicities would be accessible in reaction conditions.

For the $Rh_{10}O_n$ + CO → $Rh_{10}O_{n-1}$ + CO_2 reactions, the relative energy of the O···CO intermediate. Structure was found to be remarkably consistent as the oxidation of the Rh_{10} cluster increased, lying between −1.93 and −1.67 eV below the energy of the reactants. Similarly, the relative energy of the $Rh_{10}O_{n-1}$ product was found to lie in a narrow range of only 0.35 eV.

The oxygen addition reactions, $Rh_{10}O_n$ + N_2O → $Rh_{10}O_{n+1}$ + N_2, showed significantly different behaviour, with the energy of the O···N_2 intermediate rising by approximately 0.7 eV with each addition oxygen on the $Rh_{10}O_n$ cluster. The relative energy of the $Rh_{10}O_{n+1}$ product also rose significantly, by ≈0.3 eV, though a linear relationship was not seen for these species.

These reaction paths combined suggest that the rate of oxygen addition to the cluster surface is governed by both thermodynamic and kinetic effects, whereas, the rate of oxygen abstraction reaction is largely governed by access to oxygen on the cluster surface. Paths defined by the lowest energy reactant and lowest energy product show similar energetic profiles, suggesting that the experimentally observed reaction rates are unlikely to be significantly affected by the presence of a mixture of $Rh_{10}O_n$ isomers.

Author contributions

ATD, VM and OA: investigation MAA: conceptualization of this study, methodology, writing – review and editing.

Conflicts of interest

There are no conflicts to declare.

Acknowledgements

MAA is grateful to the Engineering and Physical Sciences Research Council for funding through grant no. EP/S015868/1 and HPC time *via* the UK Materials and Molecular Modelling Hub on Young, *via* grant no. (EP/T022213).

References

1 M. Bowker, Automotive catalysis studied by surface science, *Chem. Soc. Rev.*, 2008, **37**, 2204–2211.
2 Y. Jia, L. Geng, H. Zhang and Z. Luo, Dramatic Size-dependence of Rh_n^+ Clusters in Reacting with Small Hydrocarbons: Rh_3^+ Cluster Catalysis for Dehydrogenation, *ChemistrySelect*, 2022, **7**, e202203632.
3 F. Mafune, K. Koyama, T. Nagata, S. Kudoh, T. Yasuike, K. Miyajima, D. M. M. Huitema, V. Chernyy and J. M. Bakker, Structures of Rhodium Oxide Cluster Cations $Rh_7O_m^+$ (m = 4–7, 12, 14) Revealed by Infrared Multiple Photon Dissociation Spectroscopy, *J. Phys. Chem. C*, 2019, **123**, 5964–5971.
4 E. M. Cunningham, A. S. Gentleman, P. W. Beardsmore and S. R. Mackenzie, Structural isomers and low-lying electronic states of gas-phase $M^+(N_2O)_n$ (M = Co, Rh, Ir) ion-molecule complexes, *Phys. Chem. Chem. Phys.*, 2019, **21**, 13959–13967.
5 D. Harding, M. S. Ford, T. R. Walsh and S. R. Mackenzie, Dramatic size effects and evidence of structural isomers in the reactions of rhodium clusters, $Rh_n^{\pm}$, with nitrous oxide, *Phys. Chem. Chem. Phys.*, 2007, **9**, 2130–2136.
6 J. A. Alonso, Electronic and Atomic Structure, and Magnetism of Transition-Metal Clusters, *Chem. Rev.*, 2000, **100**, 637–678.
7 M. B. Knickelbein, Reactions of Transition Metal Clusters with Small Molecules, *Annu. Rev. Phys. Chem.*, 1999, **50**, 79–115.
8 P. Armentrout, Reactions and Thermochemistry of Small Transiton Metal Cluster Ions, *Ann. Rev. Phys. Chem.*, 2001, **52**, 423–461.
9 P. Granger and G. Leclercq, Reduction of N_2O by CO over Ceria-Modified Three-Way Pt-Rh Catalysts: Kinetic Aspects, *J. Phys. Chem. C*, 2007, **111**, 9905–9913.
10 S. M. Hamilton, W. S. Hopkins, D. J. Harding, T. R. Walsh, M. Haertelt, C. Kerpal, P. Gruene, G. Meijer, A. Fielicke and S. R. Mackenzie, Infrared-Induced Reactivity of N_2O on Small Gas-Phase Rhodium Clusters, *J. Phys. Chem. A*, 2011, **115**, 2489–2497.
11 P. Rodrguez-Kessler and A. Rodrguez-Domnguez, N_2O dissociation on small Rh clusters: A density functional study, *Comput. Mater. Sci.*, 2015, **97**, 32–35.
12 R. Aviles, E. Poulain, O. Olvera-Neria and V. Bertin, The spin significance in the capture and activation of N_2O by small Rh nanoparticles, *J. Mol. Catal. A: Chem.*, 2013, **376**, 22–33.
13 F. Mafune, J. M. Bakker and S. Kudoh, Dissociative adsorption of NO introduces flexibility in gas phase Rh_6^+clusters leading to a rich isomeric distribution, *Chem. Phys. Lett.*, 2021, **780**, 138937.
14 J.-J. Chen, Q.-Y. Liu, S.-D. Wang, X.-N. Li and S.-G. He, Catalytic NO Reduction by NO Pre-Adsorbed $RhCeO_2NO^-$ Clusters, *Chem. Phys. Chem.*, 2023, **24**, e202200743.
15 T. Nagata, S. Kudoh, K. Miyajima, J. M. Bakker and F. Mafune, Adsorption of Multiple NO Molecules on Rh_n^+ (n = 6, 7) Investigated by Infrared Multiple Photon Dissociation Spectroscopy, *J. Phys. Chem. C*, 2018, **122**, 22884–22891.
16 T. Nagata, K. Koyama, S. Kudoh, K. Miyajima, J. M. Bakker and F. Mafune, Adsorption Forms of NO on Rh_n^+ (n = 6-16) Revealed by Infrared Multiple Photon Dissociation Spectroscopy, *J. Phys. Chem. C*, 2017, **121**, 27417–27426.
17 M. J. Piotrowski, P. Piquini, Z. Zeng and J. L. F. Da Silva, Adsorption of NO on the Rh_{13}, Pd_{13}, Ir_{13}, and Pt_{13} Clusters: A Density Functional Theory Investigation, *J. Phys. Chem. C*, 2012, **116**, 20540–20549.
18 H. Xie, M. Ren, Q. Lei, W. Fang and F. Ying, Explore the Catalytic Reaction Mechanism in the Reduction of NO by CO on the Rh_7^+ Cluster: A Quantum Chemical Study, *J. Phys. Chem. C*, 2012, **116**, 7776–7781.
19 J.-D. Lee, W.-P. Fang, C.-S. Li and C.-H. Cheng, Catalytic reduction of nitrous oxide by carbon monoxide in the presence of rhodium carbonyl and hydroxide. Evidence for an electron-transfer and an oxygen-transfer mechanism, *J. Chem. Soc., Dalton Trans.*, 1991, 1923–1927.
20 S. L. Romo-Ávila and R. A. Guirado-López, Adsorption of Nitric Oxide on Small Rhn± Clusters: Role of the Local Atomic Environment on the Dissociation of the N-O Bond, *J. Phys. Chem. A*, 2012, **116**, 1059–1068.
21 J. M. Bakker and F. Mafuné, Zooming in on the initial steps of catalytic NO reduction using metal clusters, *Phys. Chem. Chem. Phys.*, 2022, **24**, 7595–7610.
22 P. Ghosh, R. Pushpa, S. de Gironcoli and S. Narasimhan, Interplay between bonding and magnetism in the binding of NO to Rh clusters, *J. Chem. Phys.*, 2008, **128**, 194708.
23 H. Yoshida, K. Koizumi, M. Boero, M. Ehara, S. Misumi, A. Matsumoto, Y. Kuzuhara, T. Sato, J. Ohyama and M. Machida, High Turnover Frequency CO–NO Reactions over Rh Overlayer Catalysts: A Comparative Study Using Rh Nanoparticles, *J. Phys. Chem. C*, 2019, **123**, 6080–6089.
24 A. Dutta and P. Mondal, Density Functional Study on Structure and Bonding Nature of CO Adsorbed $Rh_n^{\pm}$ (n = 2–8) Clusters, *J. Cluster Sci.*, 2017, **28**, 2601–2622.
25 J.-J. Chen, X.-N. Li, L.-H. Mou, Q.-Y. Liu and S.-G. He, Catalytic conversion of NO and CO into N_2 and CO_2 by rhodium-aluminum oxides in the gas phase, *J. Mater. Chem. A*, 2022, **10**, 6031–6037.

26 A. C. Hermes, S. M. Hamilton, W. S. Hopkins, D. J. Harding, C. Kerpal, G. Meijer, A. Fielicke and S. R. Mackenzie, Effects of Coadsorbed Oxygen on the Infrared Driven Decomposition of N_2O on Isolated Rh_5^+ Clusters, *J. Phys. Chem. Lett.*, 2011, **2**, 3053–3057.

27 Y. Zhang, M. Yamaguchi, K. Kawada, S. Kudoh, O. Lushchikova, V. J. M. Bakker and F. Mafune, Adsorption Forms of NO on Iridium-Doped Rhodium Clusters in the Gas Phase Revealed by Infrared Multiple Photon Dissociation Spectroscopy, *J. Phys. Chem. A*, 2022, **126**, 36–43.

28 L. Zhao, J. Du and G. Jiang, Reduction Reaction of Nitric Oxide on the Rh_5V^+ Cluster: A Density Functional Theory Mechanistic Study, *J. Phys. Chem. C*, 2019, **123**, 24495–24500.

29 K. Koyama, T. Nagata, S. Kudoh, K. Miyajima, D. M. M. Huitema, V. Chernyy, J. M. Bakker and F. Mafune, Geometrical Structures of Partially Oxidized Rhodium Cluster Cations, $Rh_6O_m^+$ (m = 4, 5, 6), Revealed by Infrared Multiple Photon Dissociation Spectroscopy, *J. Phys. Chem. A*, 2016, **120**, 8599–8605.

30 M. A. Addicoat, M. A. Buntine, B. Yates and G. F. Metha, Associative versus dissociative binding of CO to 4d transition metal trimers: A density functional study, *J. Comput. Chem.*, 2008, **29**, 1497–1506.

31 M. A. Addicoat, K. F. Lim and G. F. Metha, Reactions of Nb_2 and Nb_3 with CO, D_2, N_2, and O_2: Reconciling experimental kinetics with density functional theory-calculated reaction profiles, *J. Chem. Phys.*, 2012, **137**, 034301.

32 J. Song, Y. Quan, Y. Zhao and G. Wang, Infrared spectroscopic and density functional theoretical study on the binary rhodium-oxygen $Rh_2O_9^+$ cation, *Chem. Phys. Lett.*, 2021, **780**, 138926.

33 Y. Shi and K. M. Ervin, Catalytic oxidation of carbon monoxide by platinum cluster anions, *J. Chem. Phys.*, 1998, **108**, 1757–1760.

34 F. Zaera and C. S. Gopinath, Evidence for an N_2O intermediate in the catalytic reduction of NO to N_2 on rhodium surfaces, *Chem. Phys. Lett.*, 2000, **332**, 209–214.

35 H. Yamamoto, K. Miyajima, T. Yasuike and F. Mafuné, Reactions of Neutral Platinum Clusters with N_2O and CO, *J. Phys. Chem. A*, 2013, **117**, 12175–12183.

36 E. Hernandez, V. Bertin, J. Soto, A. Miralrio and M. Castro, Catalytic Reduction of Nitrous Oxide by the Low-Symmetry Pt_8 Cluster, *J. Phys. Chem. A*, 2018, **122**, 2209–2220.

37 C. Adlhart and E. Uggerud, C–H activation of alkanes on Rh_n^+.(n = 1–30) clusters: Size effects on dehydrogenation, *J. Chem. Phys.*, 2005, **123**, 214709.

38 J. L. F. Da Silva, M. J. Piotrowski and F. Aguilera-Granja, Hybrid density functional study of small Rh_n (n = 2–15) clusters, *Phys. Rev. B: Condens. Matter Mater. Phys.*, 2012, **86**, 125430.

39 M. K. Beyer and M. B. Knickelbein, Electric deflection studies of rhodium clusters, *J. Chem. Phys.*, 2007, **126**, 104301.

40 A. Yamada, K. Miyajima and F. Mafune, Catalytic reactions on neutral Rh oxide clusters more efficient than on neutral Rh clusters, *Phys. Chem. Chem. Phys.*, 2012, **14**, 4188–4195.

41 M. Addicoat and G. Metha, Kick: Constraining a stochastic search procedure with molecular fragments, *J. Comput. Chem.*, 2009, **30**, 57–64.

42 M. A. Addicoat, S. Fukuoka, A. J. Page and S. Irle, Stochastic structure determination for conformationally flexible heterogenous molecular clusters: Application to ionic liquids, *J. Comput. Chem.*, 2013, **34**, 2591–2600.

43 S. Grimme, C. Bannwarth and P. Shushkov, A Robust and Accurate Tight-Binding Quantum Chemical Method for Structures, Vibrational Frequencies, and Noncovalent Interactions of Large Molecular Systems Parametrized for All *spd*-Block Elements (Z = 1–86), *J. Chem. Theory Comput.*, 2017, **13**, 1989–2009.

44 R. Rüger, M. Franchini, T. Trnka, A. Yakovlev, E. van Lenthe, P. Philipsen, T. van Vuren, B. Klumpers and T. Soini, SCM, Theoretical Chemistry, Vrije Universiteit, Amsterdam, The Netherlands, *AMS 2022.1*, 2023, **https://www.scm.com**.

45 A. D. Becke, Density-functional exchange-energy approximation with correct asymptotic behavior, *Phys. Rev. A: At., Mol., Opt. Phys.*, 1988, **38**, 3098–3100.

46 J. P. Perdew, Density-functional approximation for the correlation energy of the inhomogeneous electron gas, *Phys. Rev. B: Condens. Matter Mater. Phys.*, 1986, **33**, 8822–8824.

47 J. Tao, J. P. Perdew, V. N. Staroverov and G. E. Scuseria, Climbing the Density Functional Ladder: Nonempirical Meta-Generalized Gradient Approximation Designed for Molecules and Solids, *Phys. Rev. Lett.*, 2003, **91**, 146401.

48 S. Grimme, J. Antony, S. Ehrlich and H. Krieg, A consistent and accurate ab initio parametrization of density functional dispersion correction (DFT-D) for the 94 elements H-Pu, *J. Chem. Phys.*, 2010, **132**, 154104.

49 S. Grimme, S. Ehrlich and L. Goerigk, Effect of the damping function in dispersion corrected density functional theory, *J. Comput. Chem.*, 2011, **32**, 1456–1465.

50 P. Mori-Sánchez, A. J. Cohen and W. Yang, Many-electron self-interaction error in approximate density functionals, *J. Chem. Phys.*, 2006, **125**, 201102.

51 D. J. Harding, P. Gruene, M. Haertelt, G. Meijer, A. Fielicke, S. M. Hamilton, W. S. Hopkins, S. R. Mackenzie, S. P. Neville and T. R. Walsh, Probing the structures of gas-phase rhodium cluster cations by far-infrared spectroscopy, *J. Chem. Phys.*, 2010, **133**, 214304.